energy&fuels

Article

Cite This: Energy Fuels 2018, 32, 10228−10241

pubs.acs.org/EF

Key Modeling Aspects in the Simulation of a Quasi-industrial 20 kW Moderate or Intense Low-oxygen Dilution Combustion Chamber

M. Ferrarotti,*[,†,‡,§] M. Fürst,[†,§] E. Cresci,[∥] W. de Paepe,[‡] and A. Parente*[,†,§]

[†]Université Libre de Bruxelles, École polytechnique de Bruxelles, Aero-Thermo-Mechanics Laboratory, 1050 Bruxelles, Belgium

[‡]Thermal Engineering and Combustion Unit, Université de Mons (UMONS), 7000 Mons, Belgium

[§]Combustion and Robust Optimization Group (BURN), Université Libre de Bruxelles and Vrije Universiteit Brussel, 1050 Bruxelles, Belgium

[∥]WS Warmeprozesstechnik GmbH, 71272 Renningen, Germany

ABSTRACT: A numerical and experimental investigation of a quasi-industrial furnace operating in moderate or intense low-oxygen dilution combustion regime, and fed with natural gas, is presented. The study analyzes the effect of various parameters, including the combustion model [eddy dissipation concept (EDC) and partially stirred reactor (PaSR)], the definition of the chemical and mixing time scale, the turbulence model, and the choice of the kinetic mechanism. The numerical results are validated against in-flame temperature profiles, pollutant emission, and OH* chemiluminescence images. It was found that EDC fails in providing a reasonable estimation of the ignition region, while improved predictions can be obtained using the PaSR model. A sensitivity analysis was carried out to determine the optimal mixing time scale formulation for the PaSR model. Indeed, a static time scale approach, based on defining a prescribed fraction of the integral time scale, was compared to a dynamic mixing time scale formulation, based on the ratio between the variance of the mixture fraction and its dissipation rate. Results indicate the need to modify the coefficients appearing in the scalar dissipation rate transport equation, as the latter was originally derived for homogeneous turbulence and two-dimensional configurations. Results obtained with an optimized set of transport equation coefficients are in good agreement with the experimental data and in line with those obtained calibrating the mixing constant, C_{mix}, in the static approach.

1. INTRODUCTION

Energy is undoubtedly the single most important factor impacting the prosperity of our society. Global energy consumption is predicted to continue increasing, and at least 60% of the world's energy will still be provided by combustion of bio- and fossil-derived fuels in 2040.[1] As a consequence, new breakthroughs in clean energy are needed to face the challenge of energy shortage and limited fossil fuel resources. In particular, the development of a fuel-flexible, efficient, and environmentally friendly combustion technology appears to be crucial. Among them, flameless or Moderate or Intense Low-oxygen Dilution (MILD) combustion[2,3] or Colorless Distributed Combustion (CDC)[4] has attracted increasing attention. It is characterized by diluted reactants, non-visible flame, and uniform distributed temperatures.[5,6] As a consequence, complete and efficient combustion can be assured, together with a strong reduction of pollutants, such as CO,[7] NO_x,[2,8] and soot. However, what makes such technology very attractive is the large fuel flexibility. Indeed, the process allows burning, in a clean way, even low-calorific gases in industrial conditions (such as those derived from biomass gasification).[9,10] Colorado et al.[11] investigated the effect of biogas on the performance of an experimental furnace equipped with a self-regenerative flameless burner and compared the results to the performance of the system fired with natural gas. Results showed that the temperature field and uniformity are similar for both fuels, although biogas temperatures were slightly lower as a result of the larger amount of inert gases (CO_2) in the reactants.

The potential of MILD combustion in terms of energy efficiency and pollutant emissions has been thoroughly investigated by several authors, such as Katsuki and Hasegawa,[12] Cavaliere et al.,[3,13] Khalil and Gupta,[14] and valuable knowledge has been obtained to clarify the fundamental mechanisms governing such a combustion technology. At the same time, in the last few decades, different laboratory-scale model burners were built to emulate MILD combustion. Among them, the Adelaide Jet in Hot Co-flow (AJHC) burner[15] and the Delft Jet in Hot Co-flow (DJHC)[16] have received significant attention from the combustion community, serving as reference data sets for the validation of turbulent combustion models. Recently, efforts have been spent to develop systems that can more faithfully reproduce the conditions met in realistic applications, bridging the gap from laboratory to pilot[17] and industrial scale.[18] The advantage of performing experiments on industrial systems is associated with the more realistic conditions, namely, the realistic burner design and the relevance of heat transfer effects (to the furnace walls and to colder surface representing the load). In particular, Xing et al.[19] evaluated the possibility of using liquid biofuels, diesel, and kerosene fuels for gas turbine applications, concluding that MILD combustion can potentially substitute convectional gas turbine combustion. Fortunato et

Special Issue: SMARTCATs COST Action

Received: March 28, 2018
Revised: September 9, 2018
Published: October 5, 2018

DOI: 10.1021/acs.energyfuels.8b01064
Energy Fuels 2018, 32, 10228−10241

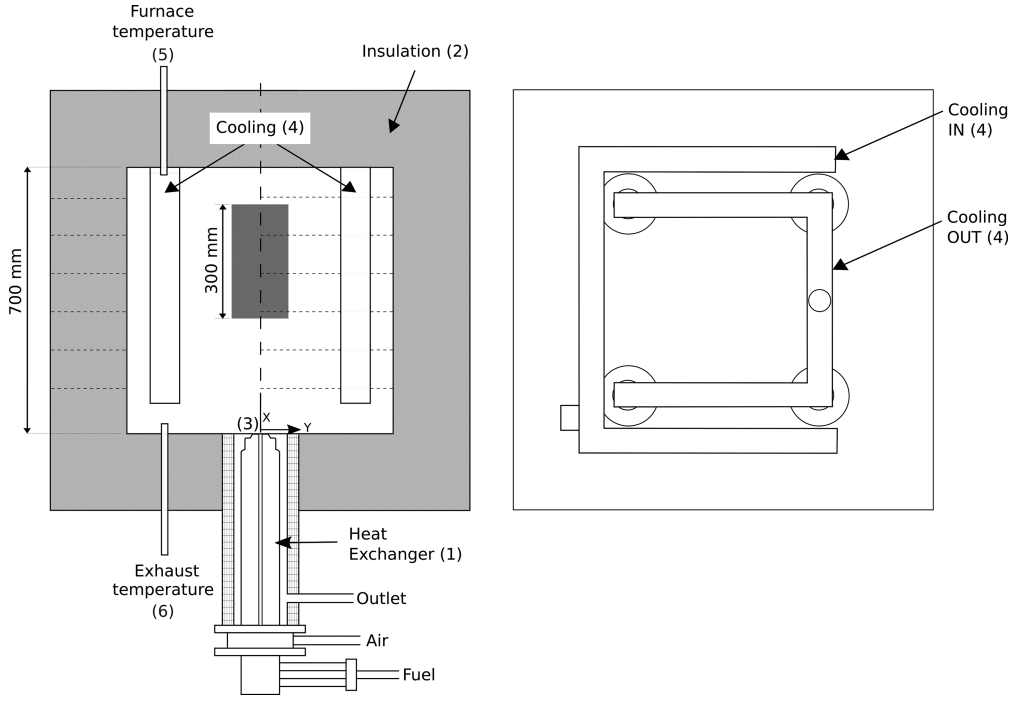

Figure 1. Schematic diagram of the MILD combustion furnace: (left) section and (right) top view. The dark gray area is the region interested by the OH* chemiluminescence imaging. Units: millimeters.

al.[20] investigated the applicability of MILD combustion for cogeneration in a Stirling engine. Mi et al.[21] studied the influences of the air−fuel injection momentum rate and the air−fuel premixing on MILD combustion in a 20 kW recuperative furnace, both numerically and experimentally. Their study suggested that there is a critical momentum rate of the inlet fuel−air mixture below which MILD combustion cannot occur. Furthermore, Adamczyk et al.[22] analyzed the potential of oxy-MILD combustion for large-scale pulverized coal boilers. Preliminary simulations showed the possibility of an efficiency increase higher than 3%. Despite the reasonable number of studies in the literature listed above, the amount of detailed experimental data available for combustors operating under MILD conditions is relatively scarce and limited to few operating conditions. On the basis of such consideration, the present study shows an experimental campaign on a quasi-industrial flameless burner operating with natural gas. Measurements involve in-flame temperature profiles thanks to a suction pyrometer, OH* chemiluminescence imaging, and pollutant concentration at the outlet.

The distinguishing feature of MILD combustion is the very strong interactions between chemical kinetics and fluid mixing, so that models based on the scale separation between turbulence and chemistry will fail in predicting the main features of such a combustion regime.[23] Therefore, models that account for finite-rate chemistry must be considered. The present work employs unsteady Reynolds-averaged Navier−Stokes (URANS) simulations in combination with a partially stirred reactor (PaSR)[24] model for turbulence/chemistry interactions. In PaSR, the interaction between turbulence and chemistry is represented with a factor κ, which is defined as the ratio between the chemical time scale and the sum of mixing and chemical scales. Furthermore, the combustion process is modeled as a sequence of reaction and mixing processes in locally uniform regions. Both the chemical, τ_c and mixing, τ_{mix}, time scales are explicitly considered in PaSR, to determine the extension and residence time of the reacting structures. Therefore, its performances strongly depend upon the accurate estimation of those scales. With regard to the chemical time scale, Chomiak[24] estimated it as using the fuel and oxidizer formation rates, while Li et al.[25] compared different approaches based on the use of formation and reaction rates and the decomposition of the Jacobian matrix of the species reaction rates. As for the mixing scale, different formulations have been proposed in the literature for τ_{mix}, ranging from Kolmogorov to the integral time scale[24,26] by means of a mixing constant C_{mix}. Sensitivity analysis on C_{mix} were conducted in the framework of probability density function (PDF) simulations for both premixed[27,28] and non-premixed flames.[29−31] Furthermore, Kuron et al.[32] invoked the adaption of a dynamic model, given the wide observed variability in the optimal choice of C_{mix}. Raman and Pitsch[33] adopted a dynamic model based on scalar variance $\tilde{\phi}''^2$ and dissipation rate $\tilde{\varepsilon}_\phi$ of a generic scalar ϕ, which automatically defines the scalar mixing time scale. Different formulations were proposed in the literature to model $\tilde{\varepsilon}_\phi$. In the present study, some of those[34−36] are compared on the basis of a review by Sanders and Gökalp.[37] To the best knowledge of the authors, no previous study was carried out to compare the available approaches for mixing and chemical time scale evaluation in the frameworks of URANS for a quasi-industrial burner.

The objective of the present paper is to provide a joint experimental and numerical analysis of a quasi-industrial furnace, applying a finite-rate combustion model coupled with an advanced mixing model. First, an overview of the experimental facility is presented, and then a preliminary analysis based on a two-dimensional (2D) axisymmetric domain is discussed. Finally, a detailed study on the full three-dimensional (3D) geometry is presented and benchmarked with experimental data of in-flame temperature, pollutant emissions, and OH* chemiluminescence measurements.

DOI: 10.1021/acs.energyfuels.8b01064
Energy Fuels 2018, 32, 10228−10241

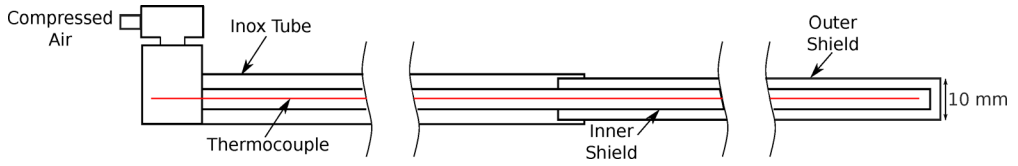

Figure 2. Schematic diagram of the suction pyrometer.

2. EXPERIMENTAL SECTION

In the following subsections, the experimental facility is presented with particular focus on the description of the operating conditions and the main measurement techniques.

2.1. Furnace. The MILD combustion furnace, used for the study presented in this paper, has a nominal power of 20 kW and shows similarities with industrial furnaces. The setup allows for the variation of the injection profiles, air excess, fuel and air velocity, and internal load (see Figure 1). Moreover, the burner has an integrated metallic finned heat exchanger (1) to extract energy from the flue gases and to preheat the combustion air. The combustion chamber itself is made of stainless steel and has a cubic internal section of 700 mm on each side. It is well-insulated with 200 mm thick high-temperature ceramic fiberboards (2), which limits the heat lost through the walls to about 15%. This assists in the establishment and stability of the MILD regime. Fuel and air are fed coaxially into the combustion chamber (3) through separated jets. The unit is equipped with an air cooling system (4) consisting of four cooling tubes [outer diameter (OD) of 80 mm], with a length of 630 mm inside the furnace. Varying the air flow allows the combustion chamber to operate at different stable conditions, thus simulating the effect of a variable load. On each vertical wall of the combustion chamber, an opening is available for measurements. One side is equipped with a 150 mm × 150 mm quartz window, which can be placed in up to two different positions along the opening length, as described by Figure 1.

2.2. Experimental Measurements. The position and shape of the reaction/heat release zone were identified via OH* chemiluminescence imaging, using an intensified charge-coupled device (ICCD) camera, 1.4 megapixels, coupled with an ultraviolet (UV) bandpass filter (240–400 nm). The charge-coupled device (CCD) sensor is equipped with 1392 × 1040 pixels each sized to 6.45 × 6.45 μm with a frame rate of 17 fps. The setup can be moved along the three axes thanks to a movable structure coupled with three stepper motors. The intensifier (IRO) gain was set to 80 coupled with a multishot technique, allowing for the capture of eight shots per frame at a frequency of 180 Hz. The gate (time between two successive bursts) was set to 999 μs. Particular attention was paid to ensure that the CCD camera exposure time (time that the sensor remains open) exceeds the sum of the integration time and delays. A series of 30 frames was taken at a global acquisition frequency of 12 Hz. The global OH* profile was constructed from images taken at two different positions of the window along the x axis, from 295 to 595 mm in the vertical direction. Before proceeding with the post-processing, the background noise was removed. The latter was recorded just after switching off the fuel injection. An averaged image and the related standard deviation were then extracted and normalized as a function of the maximum counts.

Next to the OH* chemiluminescence, the temperature inside the chamber was also measured at different locations in the furnace. The three other sides of the furnace are closed with insulated plates. In one of those, six equally spaced thermocouple ports, at a related distance of 100 mm, are installed. In particular, an air-cooled suction pyrometer equipped with a 1.5 mm diameter N-type thermocouple (Nicrosil/Nisil) is used to measure the in-flame temperature profiles. It works with a Venturi tube connected to a compressed air circuit at a maximum pressure of 6 bar(g). The thermocouple is protected from chemical attack and from radiation heat exchange with the surrounding walls by two concentric sintered alumina shields. The inox part of the probe has a diameter of 12 mm (Figure 2), while the outer ceramic shield has a diameter of 10 mm. The injector, driven by compressed air, ensures suction of gases at a high speed (≈100 m/s), which heats the thermocouple tip via convective heat transfer, so that the equilibrium thermocouple temperature is nearly that of the gases without the need for correction. The associated response time is about 10 s. The differential voltage signal is continuously sampled at 10 Hz and automatically converted to temperature units with a National Instrument cold-junction compensated acquisition card. According to the specifications of the manufacturer, the associated uncertainty is 0.75% of the reading. On the other side of the furnace, six K-type thermocouples are mounted, flush against the insulation, to measure the inner roof wall temperature. Finally, the furnace temperature (5 in Figure 1; T_f), used as a set point for the burner on/off regulation, and the flue gas temperature (6 in Figure 1; T_{fg}) are given by two shielded N-type thermocouples positioned on the central plane and shifted to 250 mm with respect the axis, on the top and bottom walls of the chamber, respectively.

Finally, the different mass flow rates entering and leaving the furnace and the composition of the flue gases are also measured. The flow rates of combustion air and cooling air are measured with thermal mass flow meters (accuracy of 0.9% of the set point). Exhaust gas composition is measured with electrochemical sensors with nominal accuracies for CO (±2 ppm), NO (±5 ppm), NO_2 (±5 ppm), and O_2 (±0.8% of reading) and with a non-dispersive infrared (NDIR) sensor for CO_2 (±1% of reading + 0.3%). The combustion products are cooled and filtered to remove moisture and particles before reaching the sensing cells and are thus measured on a dry basis.

2.3. Operating Conditions. In the present study, a natural gas flow rate of 1.9 Nm_3/h with 17% excess air (equivalence ratio $\Phi = 0.85$) was used. The natural gas composition can be approximated as follows, based on the daily data available from Fluxys Belgium[38]: 84.0% CH_4, 4.7% C_2H_6, 9.9% N_2 and 1.4% CO_2, on a molar basis (lower heating value of 33.5 MJ/Nm^3). The resulting Reynolds number of the fuel central jet [inner diameter (ID) of 8.2 mm] was $Re_{NG} \approx 6000$, while the air stream injection velocity was about 50 m/s. The cooling flow rate was set to reach the desired set-point temperature in the combustion chamber (T_f = 975 °C). Experiments were performed at steady-state conditions, after a warming period of about 3 h, during which the same burner was used in normal flame conditions, acting on the fluid dynamic of the injection.

3. NUMERICAL MODELING

Next to the experimental work, the operating condition was investigated and evaluated numerically, with the objective of developing a numerical model able to reproduce the main furnace features. The Reynolds-averaged Navier–Stokes (RANS)-based simulations were solved with the commercial code Fluent 17.0 by Ansys, Inc. Turbulence chemistry interactions were handled with the PaSR model, as shown in the following subsections.

3.1. PaSR Model. In the PaSR model,[24,39] the computational cell is split into two locally uniform zones: one zone where the reactions take place and another zone characterized by only mixing. The final species concentration of the cell is determined from the mass exchange between the two zones, driven by the turbulence. A conceptual drawing of the PaSR model is shown in Figure 3.

Figure 3 shows a computational cell, where Y_i^0 is the initial ith species mass fraction in the non-reactive region, $\tilde{Y}_i$ is the final averaged ith species mass fraction in the cell, and Y_i^* is the ith

DOI: 10.1021/acs.energyfuels.8b01064
Energy Fuels 2018, 32, 10228–10241

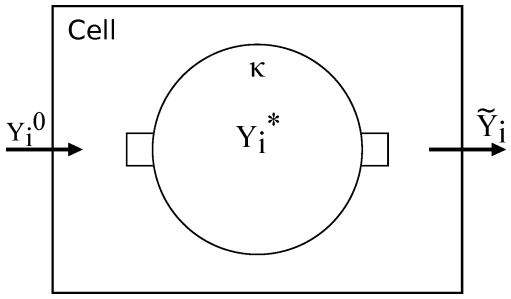

Figure 3. Conceptual drawing of the PaSR model showing the computational cell and the reactive volume fraction κ. This figure was adapted with permission from ref 25. Copyright 2018 Elsevier.

species mass fraction in the reactive zone. κ is the mass fraction of the reaction zone in the computational cell, which can be estimated as

$$\kappa = \frac{\tau_c}{\tau_c + \tau_{mix}} \tag{1}$$

where τ_c and τ_{mix} are the characteristic chemical and mixing time scales in each cell, respectively. They can be estimated following different approaches, as detailed in the following subsections. The mean source term provided to the species transport equation can be expressed as

$$\bar{\dot{\omega}}_i = \kappa \frac{\rho(Y_i^* - Y_i^0)}{\tau^*} \tag{2}$$

where ρ is the mixture density and τ^* represents the residence time in the reactive structure. In the present work, it is equal to the mixing time scale. To obtain the value of Y_i^*, a time-splitting approach is applied. The reactive zone is modeled as an ideal reactor evolving from Y_i^0 during a residence time τ^*.

$$\frac{dY_i^*}{dt} = \frac{\dot{\omega}_i^*}{\rho} \tag{3}$$

The term $\dot{\omega}_i^*$ is the instantaneous formation rate of species *i*. The final integration of dY_i^*/dt over the residence time τ^* in the reactor is Y_i^*. The PaSR formulation shows similarities with the Eddy Dissipation Concept (EDC). However, despite the fact that, in EDC, the chemical time scale depends upon the kinetic scheme, it cannot be explicitly included in the definition of κ or τ^*, unless non-standard versions are employed.[40]

3.1.1. Chemical Time Scale Evaluation. For the evaluation of the chemical time scale, Fox[41] suggested using the eigenvalues of the Jacobian matrix **J** of the chemical source terms. This approach is accurate but time-consuming, especially for large-scale simulations and detailed mechanisms, as shown by Li et al.[25] Alternatively, the chemical time scale can be obtained from the formation rates as a ratio between the local value of a species mass fraction and the corresponding formation rate.

$$\tau_{c,i} = \frac{Y_i^*}{|dY_i^*/dt|} \tag{4}$$

In eq 4, $\tau_{c,i}$ is the characteristic time scale of a single species. The slowest chemical time scale of the active species is chosen as the leading scale for the evaluation of the PaSR parameter κ after removing the dormant species (characterized by infinite time scale values). Li et al.[25] showed that this approach well approximates the chemical time scales obtained from the Jacobian matrix.

In the present work, the following sets of species are considered to calculate eq 4: 5 species (CH_4, C_2H_6, O_2, CO_2, and H_2O) and 18 species (mainly the species composing the KEE[42] mechanism, adding all of the fuel mixture species).

3.1.2. Mixing Time Scale Evaluation. In conventional combustion models (i.e., EDC), it is often assumed that reactions happen at the dissipation scales, which implies the Kolmogorov scale. However, in MILD combustion, reactions can occur over a wide range of flow scales,[23] and the use of the Kolmogorov mixing time scale could lead to inaccurate predictions of temperature and species mass fractions.[40] In the present work, two approaches are proposed. The first consists in expressing the mixing time as a certain fraction of the integral time scale by means of a constant C_{mix}, which must be conveniently selected by the user.

$$\tau_{mix} = C_{mix}\frac{k}{\varepsilon} \tag{5}$$

This constant is normally adjusted in a wide range (0.001 and 0.3).[43] A more sophisticated approach is based on the automatic definition of τ_{mix} based on local properties of the flow field using a dynamic approach.[25,33,44]

$$\tau_{mix} = \tau_\phi = \frac{\tilde{\phi}''^2}{\tilde{\varepsilon}_\phi} \tag{6}$$

In eq 6, $\tilde{\phi}''^2$ is the variance of the scalar ϕ and $\tilde{\varepsilon}_\phi$ is its dissipation rate, defined as $2D_m(\partial\tilde{\phi}''/\partial\tilde{x}_i)^2$, where D_m is the molecular diffusion coefficient. An equivalent C_{mix} can be defined as

$$C_{mix,eq} = \frac{\tau_\phi}{k/\varepsilon} \tag{7}$$

With the recognition that $C_{mix,eq}$ is not an universal constant, a dynamic estimation of a mixing time will be based on the resolution of transport equations for the scalar variance and scalar dissipation rate.[28] We base such an estimation on the mixture fraction variance and dissipation rate, in agreement with Senouci et al.[45] and Ferrarotti et al.[44] Indeed, the choice of a conserved scalar seems appropriate in the context of the PaSR modeling framework, which describes the overall process as resulting from the interaction of reacting and non-reacting structures via an exchange with the mean mechanism. The choice of the mixture fraction strongly simplifies the transport equations for $\tilde{\phi}''^2$ and $\tilde{\varepsilon}_\phi$.[41] Following refs 37 and 46, the system of transport equations can be written as

$$\frac{d\bar{\rho}\tilde{Z}''^2}{dt} = \frac{\partial}{\partial x_j}\left(\rho(D_m + D_t)\frac{\partial\tilde{Z}''^2}{\partial x_j}\right) + 2\rho D_t\left(\frac{\partial\tilde{Z}}{\partial x_j}\right)^2 - \bar{\rho}\tilde{\chi} \tag{8}$$

$$\frac{d\bar{\rho}\tilde{\chi}}{dt} = \frac{\partial}{\partial x_j}\left(\rho(D_m + D_t)\frac{\partial\tilde{\chi}}{\partial x_j}\right) - C_{D1}\bar{\rho}\frac{\tilde{\chi}^2}{\tilde{Z}''^2} - C_{D2}\bar{\rho}\frac{\tilde{\chi}\tilde{\varepsilon}}{\tilde{k}} + C_{P1}\frac{\tilde{\chi}}{\tilde{Z}''^2}P_f + C_{P2}\frac{\tilde{\chi}}{\tilde{k}}P_k \tag{9}$$

where $\bar{\rho}$ is the density of the mixture, D_t is the turbulent diffusivity, $P_f = -2\bar{\rho}\widetilde{u_k''Z''}(\partial\tilde{Z}/\partial x_k)$ is the production of scalar fluctuation, and $P_k = -2\bar{\rho}\widetilde{u_k''u_i''}(\partial\tilde{U}_i/\partial x_k)$ is the production of turbulent kinetic energy. Different approaches were tested to define the scalar dissipation rate, and the coefficient values are listed in Table 1, where $R_\tau = (k/\varepsilon)/(\tilde{Z}''^2/\chi)$ is the mechanical/

DOI: 10.1021/acs.energyfuels.8b01064
Energy Fuels 2018, 32, 10228−10241

scalar time-scale ratio. The resulting system as a result of its nature must be solved within an URANS approach.

Table 1. Values of the Coefficients in the Scalar Dissipation Rate Transport Equation[37]

author	C_{P1}	C_{P2}	C_{D1}	C_{D2}
Chen[35]	0.5	1.45	1.15	0.65
Jones and Musonge[34]	$1.7R_\tau^{-1}$	1.45	1.0	0.9

The combustion and mixing models were coupled to the main solver via a bespoke subroutine (user-defined function written in *C*).

3.2. Computational Domain and Grid. The geometry of the combustion chamber is rather complex as a result of the presence of four cooling pipes and a window. To reduce the computational time, a preliminary study was conducted using a 2D axisymmetric computational model (left side of Figure 4). A

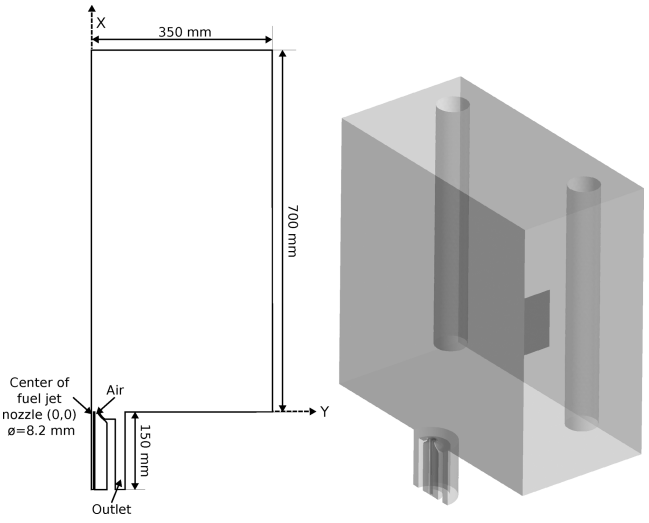

Figure 4. (Left) 2D and (right) 3D computational domain.

grid sensitivity analysis was carried out to estimate the solution error associated with the adopted discretization. To this purpose, three grids were considered, adopting a uniform coarsening ratio, ($r = h_c/h_f$), in x and y directions. The resulting number of cells ranged from about 24 000 to 96 000. The meshes were compared using PaSR with $C_{mix} = 0.1$. Following Logan and Nitta,[47] the grid convergence index (GCI) was estimated for the three grids investigated (Figure 5) based on the (a) temperature and axial velocity and (b) minor species (OH and CO). The points plotted on Figure 5 were obtained from profiles extracted along the y coordinate at different distances along the axis, i.e., x = 300, 400, 500, and 600 mm, averaging over all of the punctual errors. On the basis of Figure 5, the grid with 24 000 cells ($r = 2$) was chosen as the base mesh for the 2D numerical simulation because the GCI is always below 6% for all of the selected variables.

A 3D geometry was also considered (right side of Figure 4), simulating only a half domain as a result of the symmetry of the problem. The computational grid was first created with tetrahedrons and then converted into polyhedrons. This operation allows for the reduction of the number of cells and improvement of convergence and accuracy, because the number of neighbors is higher than those of tetrahedrons.[48] Particular attention was paid refining the fuel−air mixing zone. A grid-independency study was also performed using the eddy dissipation/finite rate (EDFR) model coupled with global chemistry, adopting a set of three grids, whose number of cells ranges from around 700 000 to 1 700 000. Figure 6 shows a

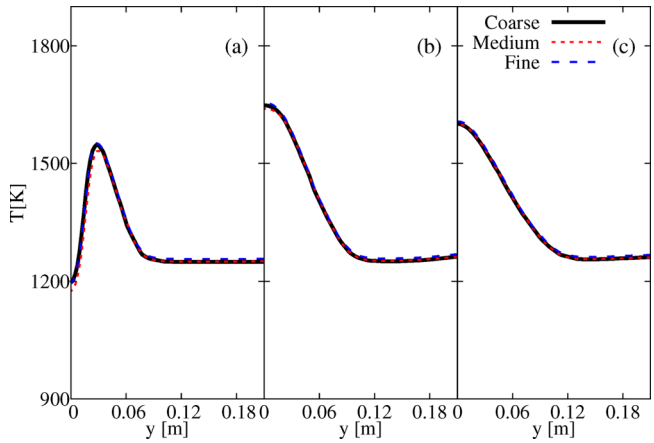

Figure 6. Grid independence based on temperature profiles at different axial locations [(a) x = 300 mm, (b) x = 400 mm, and (c) x = 500 mm] for the set of 3D grids based on the EDFR combustion model. The coarsest represents a good compromise between accuracy and CPU time.

comparison based on temperature profiles at different axial locations [(a) x = 300 mm, (b) x = 400 mm, and (c) x = 500 mm] for the set of 3D grids. The coarsest represents a good

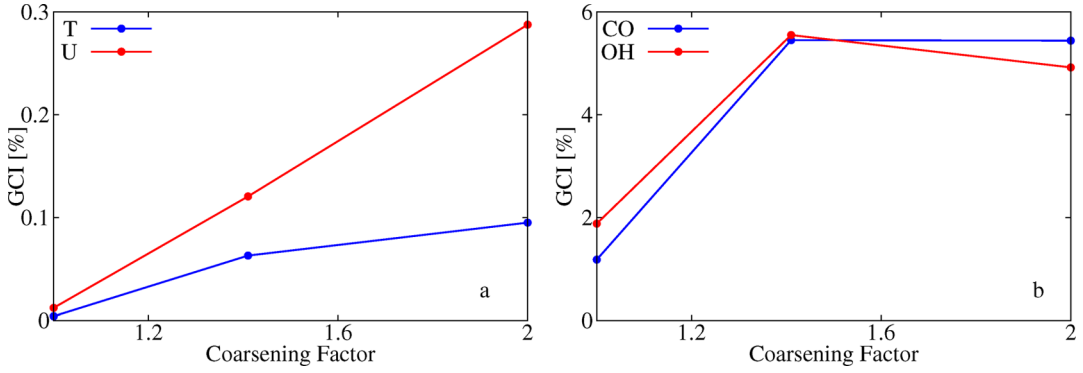

Figure 5. GCI based on (a) temperature (T) and velocity (U) and (b) CO and OH for the set of 2D grids. The coarsest ($r = 2$) represents a good compromise between accuracy and CPU time.

DOI: 10.1021/acs.energyfuels.8b01064
Energy Fuels 2018, 32, 10228−10241

compromise between accuracy and central processing unit (CPU) time, leading to a relative error always lower than 1%.

3.3. Boundary Conditions and Physical Model. Fuel was assumed to be fed into the furnace at room temperature. Because the inlet air temperature was not known from the experimental measurements, it was evaluated from an energy balance on the heat exchanger preheater. However, the exchanger effectiveness has its own uncertainty (80 ± 5%); therefore, a preliminary analysis was conducted on the 2D grid. As a consequence, the inlet air temperature varies in the range of 846−913 K for the operating condition. A low Reynolds model ($y^+ \approx 1$) was adopted for the upper wall, while standard wall functions were used for the other boundaries in the framework of enhanced wall function.[48]

In the 3D domain, the cooling surfaces were modeled using a constant negative heat flux condition, whose value is set in accordance with the furnace energy balance (see section 4.1), while the window was considered as a semi-transparent wall.[48] On the lateral walls, a conduction/convection condition was set. On the contrary, the 2D axisymmetric domain was modeled imposing the total energy losses from the real system into the lateral walls, as a constant negative heat flux.

Different kinetic schemes were considered to investigate the effect of chemistry accuracy on the results. Besides GRI-2.11[49] (31 species and 175 reactions), two reduced mechanisms were obtained from POLIMI-1412[50] according to the procedure described by Stagni et al.[51] POLIMI-25 has 25 species and 154 reactions, while POLIMI-31 has 31 species and 205 reactions. The latter also includes recombination reactions, leading to the formation of C_3H_x components. To consider the OH* radical, the sub-model (9 reactions) proposed by Panoutsos et al.[52] was added to the main kinetic schemes. Different turbulence models were also considered in the present study: standard $k-\varepsilon$ and $k-\omega$ shear-stress transport (SST) and Reynolds stress model (RSM) based on linear pressure−strain.[53] The discrete ordinate (DO) radiation model was used, in combination with the weighted-sum-of-gray-gases (WSGG) model, using the coefficients proposed by Smith et al.[54] For the URANS simulation involving the dynamic model, a time step of 10^{-4} s was chosen using a fully implicit formulation.

3.4. Validation Metric. To quantitatively measure the agreement between experimental data and computational predictions, a validation metric was employed. Following Oberkampf and Barone,[55] the expression of the estimated absolute error as a function of the input variable x is

$$\tilde{E}(x) = y_m(x) - \overline{y}_e(x) \tag{10}$$

where $y_m(x)$ is the computed value, while $\overline{y}_e(x)$ is the sample mean based on n experiments. It is possible to define an average absolute error, normalizing the absolute error by the estimated sample mean.

$$\left|\frac{\overline{E}}{\overline{y}_e}\right|_{avg} = \frac{1}{p}\sum_{i=1}^{p}\left|\frac{y_m(x_i) - \overline{y}_e(x_i)}{\overline{y}_e(x_i)}\right| = \frac{1}{p}\sum_{i=1}^{p}\left|\frac{\tilde{E}(x_i)}{\overline{y}_e(x_i)}\right| \tag{11}$$

The related confidence, CI, is determined as

$$CI = \sqrt{\left(t_{\alpha/s,\nu}\frac{s}{\sqrt{n}}\right)^2 + U_e(x)^2} \tag{12}$$

The terms under the square root in eq 12 represent the two contributions to the global uncertainty, namely, the statistical reproducibility and the experimental error. The first term is calculated assuming that the measurements follow a Student t distribution, where $t_{\alpha/s,\nu}$ is the quantile of the measured population with $\nu = n - 1$ degrees of freedom, s is the sample standard deviation, and α is the desired level of confidence. The experimental uncertainty, U_e, is estimated according to the specifications of the manufacturer for the temperature and species composition. Finally, the averaged relative error can be written as

$$\left|\frac{CI}{\overline{y}_e}\right|_{avg} = \frac{1}{p}\sum_{i=1}^{p}\left|\frac{CI_i(x_i)}{\overline{y}_e(x_i)}\right| \tag{13}$$

4. RESULTS AND DISCUSSION

In this section, the experimental energy balance is first presented. Afterward, the influence of different sub-models and model parameters on the results are discussed, including the turbulence model, kinetic scheme, and definition of the mixing and chemical time scales in the context of the PaSR model. On the basis of Table 2, one model parameter at a time is investigated. Finally, the validation of the computational approach is shown, comparing the numerical results to the available experimental data.

Table 2. Numerical Settings Used in the Present Work

combustion model	EDC and PaSR
EDC C_γ	1.9
EDC C_τ	1.47
PaSR τ_c	5 and 18 species
PaSR τ_{mix}	global and dynamic
turbulence model	standard $k-\varepsilon$, $k-\omega$ SST and RSM
kinetic scheme	GRI-2.11, POLIMI-25, and POLIMI-31
radiation model	DO−WSGG

4.1. Temperature Measurements and Energy Balance. A preliminary test was conducted to determine the sensitivity of the suction pyrometer measurements to the pressure used to induce the suction of the gases. Different pressures in the range 1−6 bar(g) were tested. Figure 7 shows that there is an asymptotic trend increasing the pressure value, implying that a

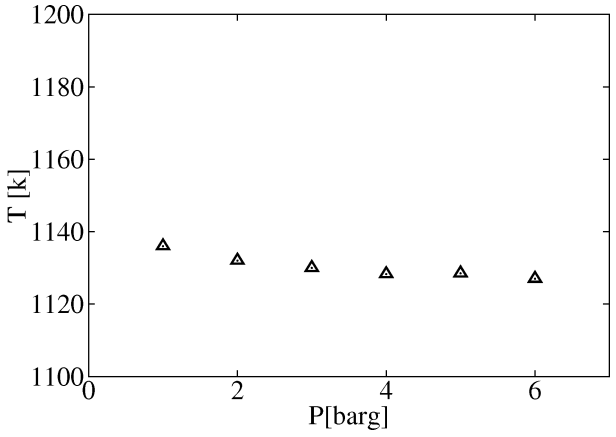

Figure 7. Sensitivity analysis based on the suction pyrometer compressed air pressure value. The temperature measurement was taken at $(x, y) = (300, 0$ mm).

DOI: 10.1021/acs.energyfuels.8b01064
Energy Fuels 2018, 32, 10228−10241

pressure of 4 bar(g) is already sufficient to reduce the error associated with the measurements.

To assess the temperature uniformity of gases inside the furnace, the relative standard deviation of the entire temperature field (uniformity ratio R_{tu}) is calculated as[17]

$$R_{tu} = \sqrt{\frac{1}{N}\sum_{i=1}^{N}\left(\frac{T_i - T_{avg}}{T_{avg}}\right)^2} \quad (14)$$

where T_{avg} is the mean temperature and N is the number of measurement points. In the present configuration, this index is equal to 0.01, with T_{avg} = 1291 K and T_{max} = 1500 K. The value of R_{tu} is in agreement with that obtained by Mosca[17] (0.035) for flameless combustion of a mixture of blast furnace gas and coke oven gas.

Table 3 shows a summary of the energy balance made on the furnace. The heat leaving the furnace through the walls was estimated after measuring the wall temperatures and taking into account natural convection on the vertical and horizontal walls (≈18% of the overall energy). The energy loss through the window (≈17%) was calculated considering the radiative energy emitted from the insulation walls (emissivity ε_w = 0.55 at 1000 °C). The amount of energy recovered by the air-cooled tubes (efficiency) was calculated using the temperature and mass flow rate measurements of the air entering and leaving the tubes; this energy output accounts for 40% of the losses.

Table 3. Energy Balance

energy input (kW)	17.6
energy loss through the wall (kW)	3.10
energy removed by the cooling tubes (kW)	7.10
energy loss through the window (kW)	3.00
energy output through the chimney (kW)	3.30
energy lost in the burner heat exchanger (kW)	1.10
efficiency (%)	40

4.2. Mass and Energy Balance Closure in the Numerical Simulations. First, a preliminary simulation was run on the 3D domain considering the EDFR combustion model to ensure the closure and agreement with experimental data of the global energy and mass balances. Figure 8 presents the measured and computed profiles of wall temperatures along the vertical direction x on the central plane. The averaged relative error is below 5%. This, together with the temperature value at the outlet reported in Table 4 (error below 1%), confirms the closure of the energy balance. A similar conclusion can be drawn for the mass balance, looking at the O_2 and CO_2 mass fractions at the outlet (Table 4).

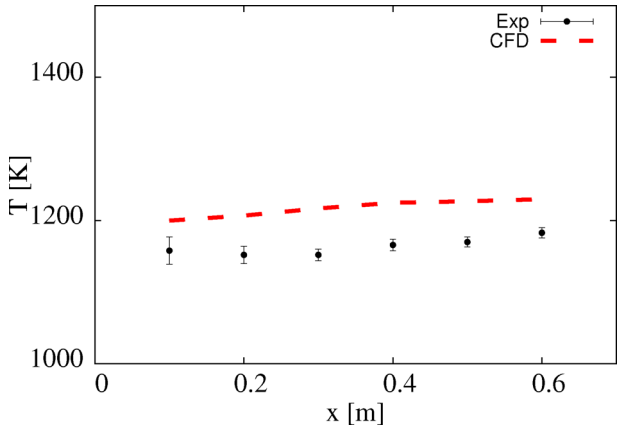

Figure 8. Comparison of the measured and computed wall temperature profiles at six different points along the x coordinate.

Table 4. Comparison of the Measured and Computed Temperature, O_2, and CO_2 (on a Dry Basis) Mole Fraction Values at the Outlet

case	T_{fg} (°C)	O_2 (%)	CO_2 (%)
exp	975 ± 7	3.30 ± 0.03	10.31 ± 0.41
CFD	973	3.32	10.01

4.3. Preliminary Analysis on the 2D Computational Domain. This section describes a preliminary analysis carried out on the 2D computational domain. In particular, first, the choice of the number of species in the evaluation of the chemical time scale is reported, followed by the sensitivity on the air inlet temperature.

4.3.1. Choice of the Number of Species in the Evaluation of the Chemical Time Scale. The first analysis conducted in the 2D domain involves the influence of the number of species selected on the estimation of the chemical time scale (see the Numerical Modeling section). Figure 9 shows a contour plot of the local chemical time scales estimated using 5 and 18 species (eq 4) with a C_{mix} = 0.1. Both species sets qualitatively and quantitatively predict the same reactive region (blue area). Therefore, a chemical time scale evaluation based on 5 species was adopted for the other simulations. This allows for the reduction of the CPU time by 15%, while keeping the averaged relative error [$\varepsilon = |(\phi_{18\ sp} - \phi_{5\ sp})/\phi_{18\ sp}|$] below 1.5% (Table 5), for different variables.

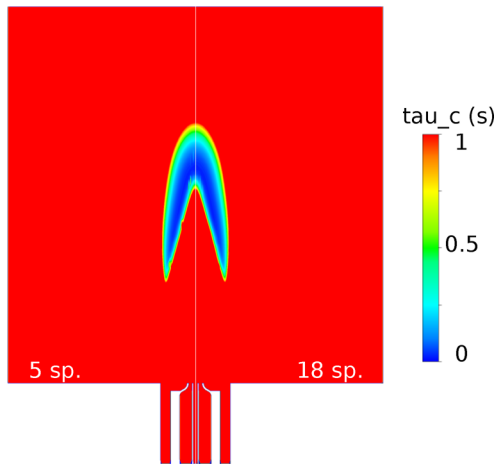

Figure 9. Chemical time scale τ_c distribution estimated using (left) 5 species and (right) 18 species. They both qualitatively and quantitatively predict the same reactive region.

4.3.2. Sensitivity on the Air Inlet Temperature. A sensitivity analysis was carried out to investigate the uncertainty related to the effectiveness of the heat exchanger, which is directly linked to the inlet air temperature value (using PaSR with C_{mix} = 0.5 and GRI 2.11). Three different effectiveness levels were tested, 75, 80, and 85%, which correspond to inlet air temperatures of 846, 879, and 917 K, respectively. Figure 10 shows the numerical profiles extracted at different axial locations. No major differences were observed between the three cases. On the

DOI: 10.1021/acs.energyfuels.8b01064
Energy Fuels 2018, 32, 10228−10241

Table 5. Percentage Averaged Error ε Adopting 5 Species for the Evaluation of τ_c

variable	ε (%)
T	0.04
U	0.03
CO	1.29
OH	0.23

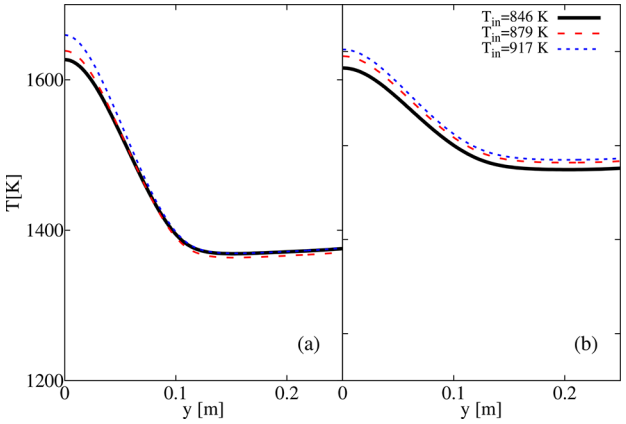

Figure 10. Sensitivity analysis based on different air inlet temperatures. Temperature profiles were obtained at (a) x = 500 mm and (b) x = 600 mm.

basis of this observation, the nominal value (80%) was considered for the subsequent simulations.

4.4. 3D Modeling Results. A detailed analysis was conducted on the 3D geometry with the aim of testing the effect of mixing, turbulence modeling, and chemistry.

Figure 11 shows the fluid dynamic features of the combustion chamber. The simulation is based on PaSR with C_{mix} = 0.3,

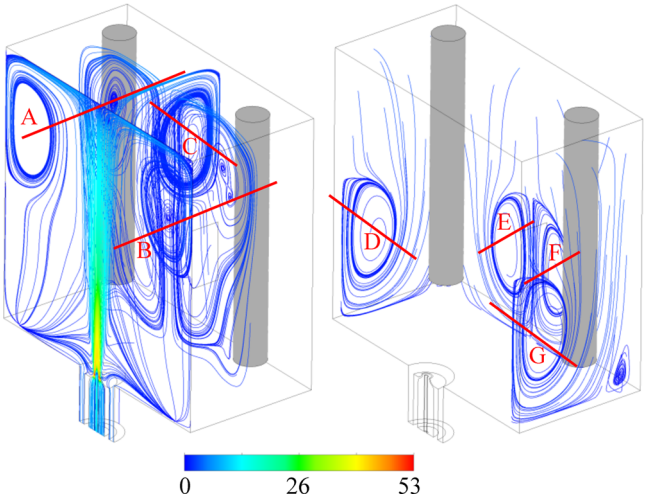

Figure 11. Streamlines, colored according to the velocity magnitude, showing the complex fluid dynamic of the 3D domain, involving a large number of vortices. Units are in meters per second.

standard $k-\varepsilon$, and GRI-2.11, while lines are colored according to velocity magnitude. The three main vortices (labeled as "A", "B", and "C") are a consequence of the impinging of the burnt gases against the upper wall. They supply continuous exhaust gases, which dilute and preheat the reactants. What makes the understanding of the flow pattern even more complex is the presence of two lateral ("D" and "G") and two interacting ("E" and "F") vortices on the back side, which might be induced by the presence of the cooling walls. The main consequence is that the heat can be dissipated and exchanged by conduction/convection in the three directions, leading to a reduction of the temperature peaks. On the other side, the axisymmetric domain of Figure 4 considers only the vortices "A" and "B", leading to a drastic simplification of the flow field.

With analysis of the recirculation zone induced by the main vortices and identification of the center of the loops, it is possible to estimate the recirculating mean velocity and density and, therefore, the recirculating flow rate ($\dot{m}_{fg}$). As a consequence, the internal recirculation degree, defined as $k_R = \dot{m}_{fg}/(\dot{m}_f + \dot{m}_a)$, was estimated to be 10, where $\dot{m}_f$ and $\dot{m}_a$ represent the fuel and mass flow rates fed to the burner, respectively. This variable was also estimated using the semi-empirical correlation proposed by Vaz[56]

$$k_R = 0.19\alpha^{1/1.36} \tag{15}$$

with $\alpha = (A_C/A_N - 1)/2$, where A_N stands for the combined area of the nozzle mouths through which fluid is injected into the chamber of the cross-sectional area A_C. Using the fuel and air gap external diameters (8.2 and 25 mm, respectively), k_R becomes equal to 15.3, which slightly overestimates the computational fluid dynamics (CFD) value. According to Wünning and Wünning,[2] the minimum k_R for MILD combustion of methane is 2.5, which clearly indicates that the furnace operates in MILD operation regime.

A large number of literature studies[40,57,58] indicate the need to modify the EDC formulation in MILD combustion by adapting the related model constants. In this study, the adjustment from Parente et al.[40] was adopted. The model constant C_γ was therefore decreased from 2.1377 to 1.9, and C_τ was increased from 0.4083 to 1.47. This setting was denoted as "EDC-2016". A comparison between PaSR with constant C_{mix} and EDC-2016 is shown in Figure 12, based on standard $k-\varepsilon$ and GRI-2.11. EDC-2016 is not able to capture the temperature distribution at any location inside the furnace, failing to provide a reasonable estimation of the ignition region location. Moreover, the reactivity predicted by EDC-2016 is quite low, because some leftover fuel is found in the fuel gases, which is not the case for

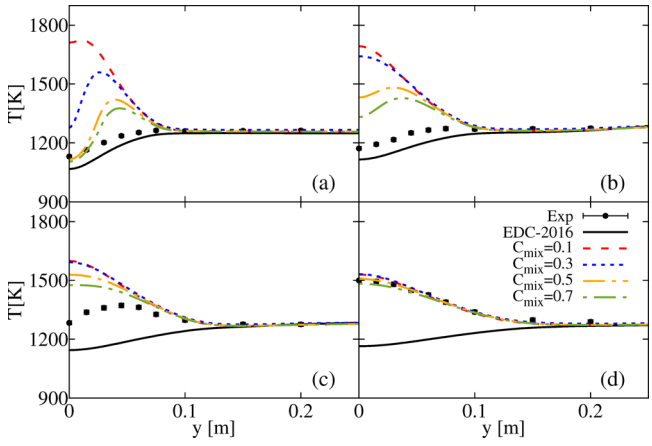

Figure 12. Comparison between PaSR and EDC-2016 in terms of mean measured and computed temperature profiles at several axial positions, namely, (a) x = 300 mm, (b) x = 400 mm, (c) x = 500 mm, and (d) x = 600 mm. Standard $k-\varepsilon$ and GRI-2.11.

DOI: 10.1021/acs.energyfuels.8b01064
Energy Fuels 2018, 32, 10228−10241

either the experiments or PaSR simulations. Figure 12 also compares the effect of varying the C_{mix} value (eq 5) on the temperature profiles obtained at different axial positions. The analysis clearly shows that the choice of this parameter is crucial to obtain reasonable results. Setting C_{mix} requires, however, *a priori* knowledge about the physics of the system. Indeed, the use of a low mixing time scale (C_{mix} = 0.1), closer to the Kolmogorov scale, results in temperature overprediction at (a) x = 300 mm, (b) x = 400 mm, and (c) x = 500 mm. Moving toward the integral time scale (C_{mix} = 0.5 and 0.7) helps to reduce the temperature overpredictions at (a) x = 300 mm and (b) x = 400 mm (global averaged error from 11.5 to 3.6% and from 16.1 to 8.4%, respectively) while providing a good match at x = 600 mm. This behavior can be confirmed quantitatively observing the values in Table 6. On the other hand, using too large values of

Table 6. Averaged Validation Metrics for Temperature Predictions, Varying the C_{mix} Constant[a]

	$\lvert\bar{E}/\bar{y}_e\rvert_{avg}$ (%)				
position (mm)	EDC-2016	C_{mix} = 0.3	C_{mix} = 0.5	C_{mix} = 0.7	$\lvert CI/\bar{y}_e\rvert_{avg}$ (%)
300	3.1	11.5	4.8	3.6	0.8
400	3.8	16.1	11.3	8.4	0.8
500	8.7	8.0	6.4	5.0	0.8
600	13.8	0.8	0.5	0.9	0.8
global	7.4	9.1	5.7	4.5	0.8

[a]Standard $k-\varepsilon$ and GRI-2.11.

C_{mix} does not allow for the prediction of the onset of the reaction, shifting the ignition toward the upper furnace wall. Analyzing Figure 12 and Figure 10, it is worth noticing the temperature reduction adopting a 3D instead of a 2D domain, for a fixed C_{mix} value. Indeed, the use of a 2D grid may result in an overestimation (up to 10%) of the temperature level. This shows that the adoption of an axisymmetric model, despite being a common practice in the literature,[59,60] is not suitable for complex 3D configurations.

The effect of the turbulence model was also studied, comparing standard $k-\varepsilon$, $k-\omega$ SST and RSM, while keeping a constant C_{mix} value (0.5). Figure 13 shows a comparison between the models, in terms of predicted temperature profiles. RSM provides a slight temperature overprediction with respect

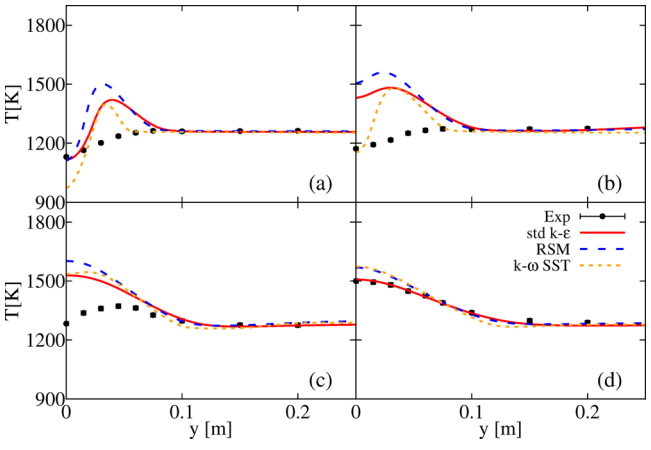

Figure 13. Sensitivity of temperature predictions to turbulence models at several axial positions, namely, (a) x = 300 mm, (b) x = 400 mm, (c) x = 500 mm, and (d) x = 600 mm. C_{mix} = 0.5 and GRI-2.11.

to standard $k-\varepsilon$ at any positions, while $k-\omega$ SST overestimates the extension of the potential core region, underpredicting the center line value at x = 300 mm. Despite this aspect, no models seem able to faithfully reproduce the ignition region, which experimentally involves a very smooth temperature gradient between x = 400 and 500 mm, , as indicated by the terms of the global averaged relative errors (Table 7). Therefore, the discrepancies observed in Figure 12 cannot be attributed to turbulence modeling.

Table 7. Averaged Validation Metrics for Temperature Predictions, Varying the Turbulence Model[a]

	$\lvert\bar{E}/\bar{y}_e\rvert_{avg}$ (%)			
position (mm)	standard $k-\varepsilon$	$k-\omega$ SST	RSM	$\lvert CI/\bar{y}_e\rvert_{avg}$ (%)
300	4.8	4.7	7.0	0.8
400	11.3	6.6	13.7	0.8
500	6.4	7.4	8.4	0.8
600	0.5	2.3	1.9	0.8
global	5.7	5.2	7.7	0.8

[a]C_{mix} = 0.5 and GRI-2.11.

Thus, the influence of the degree of accuracy of the chemical mechanism was investigated, considering other kinetic schemes, as reported in Table 2. Two reduced mechanisms (POLIMI-25 and POLIMI-31) were obtained from POLIMI-1412,[50] considering the fuel composition (CH_4, C_2H_6, CO_2, and N_2), the equivalence ratio, and the range of temperatures in the furnace. POLIMI-31 also considers hydrocarbon recombination, leading to the formation and subsequent oxidation of higher chain hydrocarbon (C_3H_x). A comparison between the two reduced POLIMI schemes and GRI-2.11 is shown in Figure 14. The two POLIMI-based schemes help to reduce the

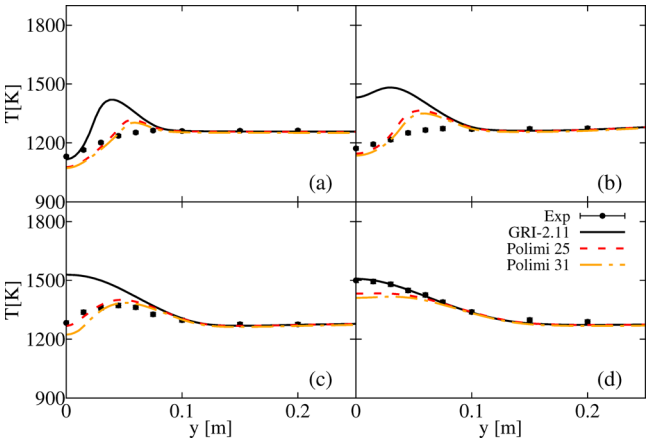

Figure 14. Sensitivity of temperature predictions to kinetic schemes at several axial positions, namely, (a) x = 300 mm, (b) x = 400 mm, (c) x = 500 mm, and (d) x = 600 mm. Standard $k-\varepsilon$ and C_{mix} = 0.5.

temperature overprediction observed with GRI-2.11 at x = 300, 400, and 500 mm. These predictions are quantitatively confirmed by the associated error metrics, always below 3% (Table 8). These results indicate that the chemical mechanisms play a major role in the predictions and confirm the limitations of GRI-based mechanisms given the low temperatures and the high turbulence intensity of the system under consideration. Indeed, such a mechanism is suited for relatively high temperatures (above 1300 K) and was found to well perform

DOI: 10.1021/acs.energyfuels.8b01064
Energy Fuels 2018, 32, 10228−10241

Table 8. Averaged Validation Metrics for Temperature Predictions, Varying the Kinetic Scheme[a]

	$\lvert\bar{E}/\bar{y}_e\rvert_{avg}$ (%)			
position (mm)	GRI-2.11	POLIMI-25	POLIMI-31	$\lvert CI/\bar{y}_e\rvert_{avg}$ (%)
300	4.8	2.4	2.4	0.8
400	11.3	3.1	2.7	0.8
500	6.4	1.4	1.9	0.8
600	0.5	2.0	2.7	0.8
global	5.7	2.3	2.4	0.8

[a] C_{mix} = 0.5; standard $k-\varepsilon$.

for a variety of cases where the system temperature is in the high-temperature range.[15,25,44,58] For the present case, given the relatively low temperatures (maximum temperature around 1500 K), the use of more comprehensive schemes can play a crucial role to reproduce the very specific features of MILD combustion (very strong turbulence/chemistry interactions and small *Da* numbers). This is not a trivial task, as proven by Sorrentino et al.[61] for similar conditions. Minor differences (around 3% on the local temperature peak at x = 500 mm) were observed between the two POLIMI-based schemes, proving that the propane pathway is not relevant under lean conditions.

With observation of Figure 12, it appears clear that the choice of C_{mix} is not trivial and requires an *a priori* knowledge of the case study. Furthermore, a constant value might not be suitable for the whole flow field. Therefore, the use of a dynamic model based on the scalar mixing time scale (eq 6) potentially offers a solution to this by providing an automatic estimation of the scalar mixing time. The two dynamic model formulations presented in Table 1, denoted as "JM" and "Chen", are compared in Figure 15 using POLIMI-25 as the kinetic scheme.

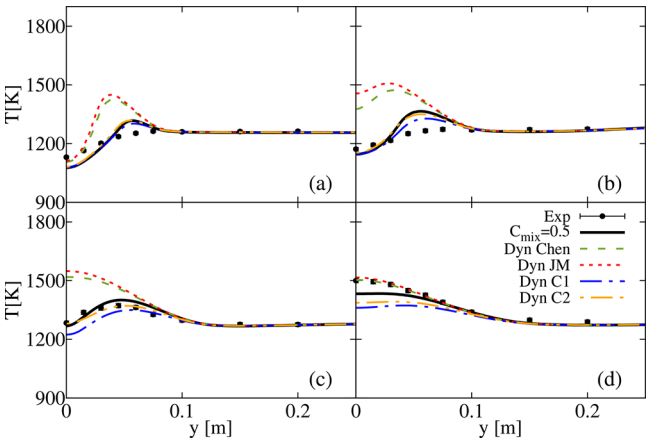

Figure 15. Effect of dynamic mixing models on computed temperature profiles at several axial positions, namely, (a) x = 300 mm, (b) x = 400 mm, (c) x = 500 mm, and (d) x = 600 mm. Standard $k-\varepsilon$ and POLIMI-25.

Both dynamic formulations show an overestimation close to the axis, for both x = 300 and 400 mm, indicating early ignition with respect to the experiments. However, the scalar dissipation transport equations proposed by Chen[35] and Jones and Musonge[34] are based on analytical considerations assuming homogeneous turbulence and 2D configurations. These assumptions are likely violated in the present case, where the flow structure is 3D and turbulence is shear-driven, as pointed out by Ye[46] in the context of a 3D turbulent non-premixed bluff-body-stabilized CH_4-H_2 flame.[62] As a consequence, the coefficients proposed by Chen[35] and Jones and Musonge[34] for the scalar dissipation rate transport equation (Table 1) might not be adequate. On the basis of this observation, we decided to carry out a sensitivity study on these coefficients, to investigate their impact on the results. In particular, C_{P1} and C_{D1}, which are associated with scalar production and destruction, were modified following the study by Ye.[46] Indeed, the gradients of mean velocity and scalar mean field differ greatly between homogeneous and inhomogeneous flow. Because, in eq 9, the production term is coupled to the gradients of the scalar mean field, while the destruction term is sensitive to the scalar variance field, the associated coefficients C_{P1} and C_{D1} were modified (doubled and halved). The new set of values, defined as cases *C*1 and *C*2, are reported in Table 9. The sensitivity study indicated

Table 9. Recalibrated Coefficients for the Scalar Dissipation Rate Equation

author	C_{P1}	C_{P2}	C_{D1}	C_{D2}
Jones and Musonge[34]	$1.7R_\tau^{-1}$	1.45	1.0	0.9
*C*1	$0.85R_\tau^{-1}$	1.45	2.0	0.9
*C*2	$1.7R_\tau^{-1}$	1.45	2.0	0.9

that the modification of the constants had an important impact on the results and led to improved predictions, as also observed by Ye.[46] In particular, using the modified values, $\tilde{\varepsilon}_\phi$ is reduced and $C_{mix,eq}$ increased, leading to reduced temperature peaks. The present results support the need for further studies focusing on the formulation of the scalar dissipation rate transport equation (whose form is still debated[33]). This is confirmed by the analysis of Figure 15, where the temperature profiles obtained with the modified dynamic approaches show very good agreement with the experimental data, in line with the results provided using the constant C_{mix} approach, after calibration. Because no major differences were found between the cases *C*1 and *C*2 (Table 9), it can be inferred that C_{D1} has a major impact on the scalar dissipation rate for the present case. These considerations can be quantitatively confirmed analyzing the error metric reported in Table 10. Indeed, the dynamic models globally provide an error lower than 3%.

The model validation is extended to the determination of the position of the normalized OH* distribution. OH* is a good marker to identify the reactive region topology and position, and it is also correlated with the heat release rate.[63] Different from CH*, its emission peak is shifted toward UV (≈300 nm), avoiding interference from radiation from the walls. Figure 16 shows a comparison between (a) measured and (b) computed contours of normalized OH* using the PaSR dynamic *C*2 model, together with the standard $k-\varepsilon$ and POLIMI-25 kinetic mechanism. The plotted area corresponds to the dark gray surface of Figure 1. Experimentally, the reactive zone appears smooth and mainly focused in an area between x = 370 and 520 mm. The contour appears not perfectly symmetric, probably as a result of a collection of causes, such as the not perfect symmetry of the heat extracted by the four cooling pipes. The distribution of OH* in the numerical simulations was estimated using the sub-mechanism proposed by Panoutsos et al.[52] This scheme considers collisional quenching and two main reactions for creation (eq 16) and destruction (eq 17) of OH*.

$$CH + O_2 \rightarrow OH^* + CO \quad (16)$$

DOI: 10.1021/acs.energyfuels.8b01064
Energy Fuels 2018, 32, 10228−10241

Table 10. Averaged Validation Metrics for Temperature Measurements, Adopting the Dynamic Model[a]

	$\lvert\overline{E}/\overline{y}_e\rvert_{avg}$ (%)				
position (mm)	dynamic Chen	dynamic JM	dynamic $C1$	dynamic $C2$	$\lvert CI/\overline{y}_e\rvert_{avg}$ (%)
300	4.8	5.5	2.1	2.3	0.8
400	10.4	12.3	2.1	2.7	0.8
500	6.3	7.1	2.0	0.7	0.8
600	0.5	0.7	4.4	3.3	0.8
global	5.5	6.4	2.7	2.3	0.8

[a]Standard $k-\varepsilon$ and POLIMI-25.

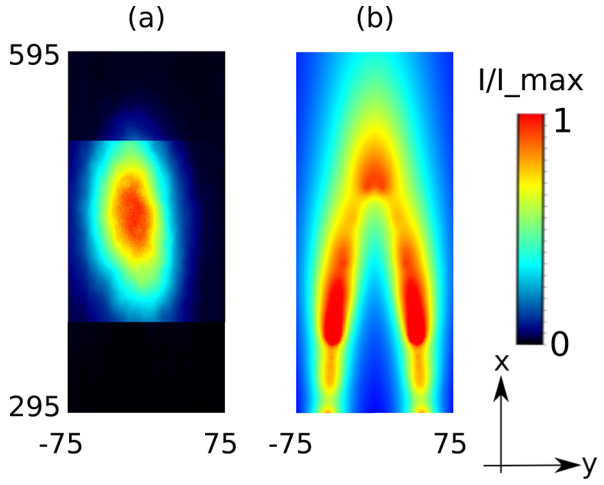

Figure 16. (a) Measured and (b) computed contours of normalized OH*. Standard $k-\varepsilon$, POLIMI-25 and dynamic $C2$. Units are in millimeters.

$$OH^* \rightarrow OH + h\nu \quad (17)$$

With the experimental OH* measurements being integrated along a line of sight, the numerical predictions of OH* were also integrated along a thickness equal to the experimental optical depth of field. The latter was estimated considering many parameters, such as the circle of confusion of the camera, the focal length and f-stop of the objective, and the distance of the camera/furnace. As a result, a value of 40 mm was estimated. In agreement with the temperature predictions in Figure 15, the modified dynamic model allows for the capture of the location in terms of the axial distance from the burner exit. However, the numerical simulations do not predict a homogeneous OH* region as in the experiments, but rather a jet-shaped region closing on the axis at the correct location. It must be stressed that this kind of validation cannot be quantitative as a result of the nature of the measurement technique, and the task is made even more complex by the fact that OH* concentrations in the numerical simulation are extremely low ($\approx 10^{-15}$). Furthermore, the OH* sub-mechanism was validated for different flame configurations, and uncertainties are associated with its use in MILD conditions.

4.5. Pollutant Emissions. Finally, a comparison between measured and predicted NO and CO emissions is reported in Table 11, corrected to 3% O_2 (by vol) in the exhausts. Considering that, in MILD combustion, the thermal pathway is not the main NO source, other routes were included, such as prompt, N_2O, and NNH. Experimentally, the authors noticed a drastic reduction of NO_x and CO switching from a conventional flame (100 and 20 ppm_v, respectively) to MILD mode (6 and 1 ppm_v, respectively), confirming the potential of MILD combustion as a low-polluting technology. Table 11 shows that the pollutant emissions are slightly underestimated.

Table 11. Measured and Predicted NO_x and CO Emissions

case	NO_x (ppm_v)	CO (ppm_v)
experiment	6 ± 5	1 ± 2
$C_{mix} = 0.5$ and POLIMI-25	1	3
dynamic $C2$ and POLIMI-25	1	<1

The causes of such underestimation might be related to the use of individual single-step mechanisms for each of the NO formation routes rather than a detailed scheme. However, it should be underlined that the task is strongly complicated by the very low amount of parts per million experimentally emitted (single digit) and the associated large experimental uncertainty.

5. CONCLUSION

A numerical and experimental investigation of a quasi-industrial furnace operating in MILD combustion regime, fed with natural gas, has been presented. The study focused on the effect of various parameters on the numerical predictions, including the combustion model (EDC and PaSR), the definition of the chemical and mixing time scale, the turbulence model and kinetic mechanisms. Numerical results were validated against experimental temperature profiles, pollutant emission and OH* chemiluminescence imaging. First, a 2D domain was considered to study the uncertainty related to the inlet air temperature value and the choice of the chemical time scale. Then, an analysis on the full 3D domain was conducted, investigating the effect of various modeling choices on the results.

The major finding can be summarized as follows: (1) The 3D and the axisymmetric model were compared. The complex fluid dynamic structure typical of the 3D geometry helps reducing the temperature peak and having a more homogeneous profile. It was found that the axisymmetric model overestimates the temperature peaks by 10% at all locations. (2) The chemical time scale was evaluated approximating the diagonal of the Jacobian matrix and considering the slowest scale of the active species. It was found that only the global species can be considered without loss of accuracy, reducing the required computational time. (3) EDC-2016 fails in providing a reasonable estimation of the ignition region for the case under investigation. Furthermore, it predicts low reactivity, with some leftover fuel in the flue gases. This might be related to the confinement of the present system and its effect on the location of the reaction region. (4) Different mixing models were tested to estimate the mixing time scale for PaSR, adopting GRI-2.11 and standard $k-\varepsilon$. First, a parametric study was conducted to determine the optimal choice of the constant C_{mix} when adopting a global mixing model. Results showed that the best compromise is obtained with a relatively high C_{mix} value (between 0.5 and 0.7). A turbulence modeling sensitivity

DOI: 10.1021/acs.energyfuels.8b01064
Energy Fuels 2018, 32, 10228−10241

analysis (standard $k-\varepsilon$, $k-\omega$ SST and RSM) was also conducted showing similar performances. Finally, the effect of the complexity of the chemical mechanism was also investigated. Two mechanisms were reduced from POLIMI-1412 for the conditions of interest and tested, namely, POLIMI-25 and POLIMI-31. They both alleviate the overprediction shown by GRI-2.11, showing good agreement with the experimental data, as demonstrated by the error metric, well below 3%. (5) Finally, a dynamic mixing model based on the resolution of transport equations for the variance and the dissipation rate of the mixture fraction was also used. It is able to automatically determine the mixing time scale without tuning any parameters. Using the scalar dissipation rate transport equations proposed by Chen[35] and Jones and Musonge,[34] temperature overestimations were observed at x = 300, 400, and 500 mm. A parametric study was carried out to investigate the effect of the transport equation coefficients on the results. In particular, the modification of the equation coefficients, aimed at reducing the scalar dissipation rate, provided improved agreement with the experiments. These results support the need for further studies focusing on the formulation of the scalar dissipation rate transport equation (whose form is still debated). (6) OH* chemiluminescence imaging was used to experimentally localize the position of the reactive/heat-released region in MILD conditions, and it was found to be in an area between x = 370 and 520 mm. Numerically, the excited radical normalized distribution can be reasonably estimated, adding an additional sub-mechanism to the main kinetic scheme. (7) The system was found to perform very well in terms of pollutant emissions, with NO_x and CO emissions well below 10 ppm.

AUTHOR INFORMATION

Corresponding Authors

*E-mail: marco.ferrarotti@ulb.ac.be.

*E-mail: alessandro.parente@ulb.ac.be.

ORCID

M. Ferrarotti: 0000-0002-3237-773X

A. Parente: 0000-0002-7260-7026

Notes

The authors declare no competing financial interest.

ACKNOWLEDGMENTS

This project has received funding from the Fonds de la Recherche Scientifique (FNRS), Belgium. The research of the second author was supported by the European Union's Horizon 2020 research and innovation program under the Marie Sklodowska-Curie grant agreement No. 643134. The research of A. Parente was sponsored by the European Research Council, Starting Grant 714605, and from the Fédération Wallonie-Bruxelles, via Les Actions de Recherche Concertée (ARC) call for 2014–2019. The authors thank the technical team at Université Libre de Bruxelles and Adrien Fita-Codina for his constant help and support in designing and optimizing the experimental facility.

NOMENCLATURE

Acronyms and Symbols

C_{mix} = mixing constant

C_{P1}, C_{P2}, C_{D1}, and C_{D2} = constants of the scalar dissipation equation

CI = experimental confidence interval

D_m = molecular diffusion coefficient

D_t = turbulent diffusion coefficient

k_R = internal recirculation degree

P_f = production of scalar fluctuation

P_k = production of turbulent kinetic energy

R_τ = mechanical/scalar time-scale ratio

R_{tu} = temperature uniformity ratio

T_{fg} = flue gas temperature

T_f = furnace temperature

U = velocity

Z = mixture fraction

AJHC = Adelaide jet in hot co-flow

CDC = colorless distributed combustion

CFD = computational fluid dynamics

CPU = central processing unit

DJHC = Delft jet in hot co-flow

DO = discrete ordinate

EDC = eddy dissipation concept

EDFR = eddy dissipation/finite rate

GCI = grid convergence index

ICCD = intensified charge-coupled device

ID = inner diameter

MILD = moderate or intense low-oxygen dilution

NDIR = non-dispersive infrared

OD = outer diameter

PaSR = partially stirred reactor

PDF = probability density function

PLIF = planar laser-induced fluorescence

Re = Reynolds number

RSM = Reynolds stress model

URANS = unsteady Reynolds-averaged Navier–Stokes

WSGG = weighted sum of gray gases

Greek and Roman Symbols

$\dot{\omega}_i$ = source term for species i

ε = dissipation of turbulence kinetic energy

ε_w = wall emissivity

κ = mass fraction of the reaction zone

Φ = equivalence ratio

ϕ = general scalar

ρ = density

τ_* = residence time in the reactive region

τ_c = chemical time scale

τ_{mix} = mixing time scale

$\tilde{\chi}$ = Favre-averaged scalar dissipation rate of the mixture fraction

$\tilde{\varepsilon}_\phi$ = Favre-averaged scalar dissipation rate

$\widetilde{\phi''^2}$ = Favre-averaged scalar variance

E = estimated absolute error

$\widetilde{Y}_i$ = averaged i_{th} species mass fraction in the cell

Y_i^0 = initial i_{th} species mass fraction in the nonreactive region

$\widetilde{Z''^2}$ = Favre-averaged scalar variance of the mixture fraction

k = turbulence kinetic energy

Y_i^* = i_{th} species mass fraction in the reactive zone

REFERENCES

(1) International Energy Agency (IEA). *Key World Energy Statistics*; IEA: Paris, France, 2017.

(2) Wünning, J. A.; Wünning, J. G. Flameless oxidation to reduce thermal NO-formation. *Prog. Energy Combust. Sci.* **1997**, *23*, 81–94.

(3) Cavaliere, A.; de Joannon, M. MILD combustion. *Prog. Energy Combust. Sci.* **2004**, *30*, 329–366.

(4) Arghode, V. K.; Gupta, A. K. Effect of flow field for colorless distributed combustion (CDC) for gas turbine combustion. *Appl. Energy* **2010**, *87*, 1631–1640.

DOI: 10.1021/acs.energyfuels.8b01064
Energy Fuels 2018, 32, 10228–10241

(5) Dally, B. B.; Riesmeier, E.; Peters, N. Effect of fuel mixture on moderate and intense low oxygen dilution combustion. *Combust. Flame* **2004**, *137*, 418−431.
(6) de Joannon, M.; Sorrentino, G.; Cavaliere, A. MILD combustion in diffusion-controlled regimes of hot diluted fuel. *Combust. Flame* **2012**, *159*, 1832−1839.
(7) Mardani, A.; Tabejamaat, S.; Hassanpour, S. Numerical study of CO and CO_2 formation in CH_4/H_2 blended flame under MILD condition. *Combust. Flame* **2013**, *160*, 1636−1649.
(8) Szegö, G. G.; Dally, B. B.; Nathan, G. J. Scaling of NO_x emissions from a laboratory-scale MILD combustion furnace. *Combust. Flame* **2008**, *154*, 281−295.
(9) Hosseini, S.; Wahid, M.; Abuelnuor, A. Biogas flameless combustion: A review. *Appl. Mech. Mater.* **2013**, *388*, 273−279.
(10) Choi, G. M.; Katsuki, M. Advanced low NO_x combustion using highly preheated air. *Energy Convers. Manage.* **2001**, *42*, 639−652.
(11) Colorado, A. F.; Herrera, B. A.; Amell, A. A. Performance of a Flameless combustion furnace using biogas and natural gas. *Bioresour. Technol.* **2010**, *101*, 2443−2449.
(12) Katsuki, M.; Hasegawa, T. The science and technology of combustion in highly preheated air. *Symp. Combust., [Proc.]* **1998**, *27*, 3135−3146.
(13) de Joannon, M.; Cavaliere, A.; Faravelli, T.; Ranzi, E.; Sabia, P.; Tregrossi, A. Analysis of process parameters for steady operations in methane MILD combustion technology. *Proc. Combust. Inst.* **2005**, *30*, 2605−2612.
(14) Khalil, A. E. E.; Gupta, A. K. On the flame−flow interaction under distributed combustion conditions. *Fuel* **2016**, *182*, 17−26.
(15) Dally, B. B.; Karpetis, A. N.; Barlow, R. S. Structure of turbulent non-premixed jet flames in a diluted hot coflow. *Proc. Combust. Inst.* **2002**, *29*, 1147−1154.
(16) Oldenhof, E.; Tummers, M. J.; van Veen, E. H.; Roekaerts, D. J. E. M. Role of entrainment in the stabilisation of jet-in-hot-coflow flames. *Combust. Flame* **2011**, *158*, 1553−1563.
(17) Mosca, G. Experimental and Numerical Study of MILD Combustion. Ph.D. Thesis, Université de Mons, Mons, Belgium, 2006.
(18) Tu, Y.; Liu, H.; Li, P.; Wang, F.; Zhang, T.; Bai, C.; Zheng, Y.; Liu, Z.; Mi, J.; Zheng, C. Experimental study of MILD combustion for pulverized coal in 0.3 MW vertical furnace. *Proceedings of the 9th Asia-Pacific Conference on Combustion*; Gyeongju, Korea, May 19−22, 2013.
(19) Xing, F.; Kumar, A.; Huang, Y.; Chan, S.; Ruan, C.; Gu, S.; Fan, X. Flameless combustion with liquid fuel: A review focusing on fundamentals and gas turbine application. *Appl. Energy* **2017**, *193*, 28−51.
(20) Fortunato, V.; Abou-Taouk, A.; Parente, A. Experimental and numerical investigation of a MILD-based Stirling engine fed with landfill gas. *Energy Procedia* **2017**, *120*, 230−237.
(21) Mi, J.; Li, P.; Dally, B. B.; Craig, R. A. Importance of initial momentum rate and air−fuel premixing on moderate or intense low oxygen dilution (MILD) combustion in a recuperative furnace. *Energy Fuels* **2009**, *23*, 5349−5356.
(22) Adamczyk, W. P.; Bialecki, R. A.; Ditaranto, M.; Gladysz, P.; Haugen, N. E. L.; Katelbach-Wozniak, A.; Klimanek, A.; Sladek, S.; Szlek, A.; Wecel, G. CFD modeling and thermodynamic analysis of a concept of a MILD-OXY combustion large scale pulverized coal boiler. *Energy* **2017**, *140*, 1305−1315.
(23) Minamoto, Y.; Swaminathan, N.; Cant, R. S.; Leung, T. Reaction zones and their structure in MILD combustion. *Combust. Sci. Technol.* **2014**, *186*, 1075−1096.
(24) Chomiak, J. *Combustion: A Study in Theory, Fact and Application*; Abacus Press/Gorden and Breach Science Publishers: Philadelphia, PA, 1990.
(25) Li, Z.; Ferrarotti, M.; Cuoci, A.; Parente, A. Finite-rate chemistry modelling of non-conventional combustion regimes using a partially-stirred reactor closure: Combustion model formulation and implementation details. *Appl. Energy* **2018**, *225*, 637−655.
(26) Li, Z.; Cuoci, A.; Sadiki, A.; Parente, A. Comprehensive numerical study of the Adelaide Jet in Hot-Coflow burner by means of RANS and detailed chemistry. *Energy* **2017**, *139*, 555−570.
(27) Raman, V.; Fox, R. O.; Harvey, A. D. Hybrid finite-volume/transported PDF simulations of a partially premixed methane−air flame. *Combust. Flame* **2004**, *136*, 327−350.
(28) Stöllinger, M.; Heinz, S. Evaluation of scalar mixing and time scale models in PDF simulations of a turbulent premixed flame. *Combust. Flame* **2010**, *157*, 1671−1685.
(29) Merci, B.; Roekaerts, D.; Naud, B. Study of the performance of three micromixing models in transported scalar PDF simulations of a piloted jet diffusion flame ("Delft Flame III"). *Combust. Flame* **2006**, *144*, 476−493.
(30) Krisman, A.; Tang, J. C.; Hawkes, E. R.; Lignell, D. O.; Chen, J. H. A DNS evaluation of mixing models for transported PDF modelling of turbulent nonpremixed flames. *Combust. Flame* **2014**, *161*, 2085−2106.
(31) Xu, J.; Pope, S. B. PDF calculations of turbulent nonpremixed flames with local extinction. *Combust. Flame* **2000**, *123*, 281−307.
(32) Kuron, M.; Hawkes, E. R.; Ren, Z.; Tang, J. C.; Zhou, H.; Chen, J. H.; Lu, T. Performance of transported PDF mixing models in a turbulent premixed flame. *Proc. Combust. Inst.* **2017**, *36*, 1987−1995.
(33) Raman, V.; Pitsch, H. A consistent LES/filtered-density function formulation for the simulation of turbulent flames with detailed chemistry. *Proc. Combust. Inst.* **2007**, *31*, 1711−1719.
(34) Jones, W. P.; Musonge, P. *Phys. Fluids* **1988**, *31*, 3589−3604.
(35) Chen, J. Y. *Combust. Flame* **1987**, *69*, 1−36.
(36) Sommer, T. P.; So, R. M. C.; Lai, Y. G. *Int. J. Heat Mass Transfer* **1992**, *35*, 3375−3387.
(37) Sanders, J. P. H.; Gökalp, I. Scalar dissipation rate modelling in variable density turbulent axisymmetric jets and diffusion flames. *Phys. Fluids* **1998**, *10*, 938−948.
(38) *Fluxys Belgium Home Page.* https://www.fluxys.com/belgium/en/About%20natural%20gas/TypesOfNaturalGas/GasLorH.
(39) Golovitchec, V. I.; Chomiak, J. Numerical modeling of high temperature air flameless combustion. *Proceedings of the 4th International Symposium on High Temperature Air Combustion and Gasification*; Rome, Italy, Nov 27−30, 2001.
(40) Parente, A.; Malik, M. R.; Contino, F.; Cuoci, A.; Dally, D. Characteristics and mechanistic analysis of CO formation in MILD regime with simultaneously diluted and preheated oxidant and fuel. *Fuel* **2016**, *163*, 98−111.
(41) Fox, O. R. *Computational Models for Turbulent Reacting Flows*; Cambridge University Press: Cambridge, U.K., 2003.
(42) Bilger, R.; Starner, S.; Kee, R. On reduced mechanisms for methane−air combustion in nonpremixed flames. *Combust. Flame* **1990**, *80*, 135−149.
(43) Nordin, P. A. N. Complex chemistry modeling of diesel spray combustion. Ph.D. Thesis, Chalmers University of Technology, Göteborg, Sweden, 2001.
(44) Ferrarotti, M.; Li, Z.; Parente, A. On the role of mixing models in the simulation of MILD combustion using finite-rate chemistry combustion models. *Proc. Combust. Inst.* **2018**, DOI: 10.1016/j.proci.2018.07.043.
(45) Senouci, M.; Bounif, A.; Abidat, M.; Belkaid, N. M.; Mansour, C.; Gokalp, I. Transported-PDF (IEM, EMST) micromixing models in a hydrogen−air nonpremixed turbulent flame. *Acta Mechanica* **2013**, *224*, 3111−3124.
(46) Ye, I. Investigation of the scalar variance and scalar dissipation rate in URANS and LES. Ph.D. Thesis, University of Waterloo, Waterloo, Ontario, Canada, 2011.
(47) Logan, R. W.; Nitta, C. K. Comparing 10 Methods for Solution Verification, and Linking to Model Validation. *J. Aerosp. Comput., Inf., Commun.* **2006**, *3*, 354−373.
(48) Ansys, Inc. *Fluent Theory Guide, Release 17.0*; Ansys, Inc.: Canonsburg, PA, 2017.
(49) Bowman, C. T.; Hanson, R. K.; Davidson, D. F.; Gardiner, W. C.; Lissianski, V.; Smith, G. P.; Golden, D. M.; Frenklach, M.; Goldenberg, M. *GRI-2.11*; http://www.me.berkeley.edu/gri_mech/.
(50) Ranzi, E.; Frassoldati, A.; Grana, R.; Cuoci, A.; Faravelli, T.; Kelley, A. P.; Law, C. K. Hierarchical and comparative kinetic modeling of laminar flame speeds of hydrocarbon and oxygenated fuels. *Prog. Energy Combust. Sci.* **2012**, *38*, 468−501.

DOI: 10.1021/acs.energyfuels.8b01064
Energy Fuels 2018, 32, 10228−10241

(51) Stagni, A.; Frassoldati, A.; Cuoci, A.; Faravelli, T.; Ranzi, E. Skeletal mechanism reduction through species-targeted sensitivity analysis. *Combust. Flame* **2016**, *163*, 382−393.
(52) Panoutsos, C. S.; Hardalupas, Y.; Taylor, A. M. Numerical evaluation of equivalence ratio measurement using OH* and CH* chemiluminescence in premixed and non-premixed methane−air flames. *Combust. Flame* **2009**, *156*, 273−291.
(53) Fu, S.; Launder, B. E.; Leschziner, M. A. Modeling Strongly Swirling Recirculating Jet Flow with Reynolds-Stress Transport Closures. *Proceedings of the Sixth Symposium on Turbulent Shear Flows*; Toulouse, France, Sept 7−9, 1987.
(54) Smith, T. F.; Shen, Z. F.; Friedman, J. N. Evaluation of Coefficients for the Weighted Sum of Gray Gases Model. *J. Heat Transfer* **1982**, *104*, 602.
(55) Oberkampf, W. L.; Barone, M. F. Measures of agreement between computation and experiment: Validation metrics. *J. Comput. Phys.* **2006**, *217*, 5−36.
(56) Vaz, D. C. Relations between global recirculation ratio and area ratio in combustors fired with jets. *Heat Proc.* **2011**, *9*, 253−255.
(57) Aminian, J.; Galletti, C.; Shahhosseini, S.; Tognotti, L. Key modeling issues in prediction of minor species in diluted- preheated combustion conditions. *Appl. Therm. Eng.* **2011**, *31*, 3287−3300.
(58) Evans, M. J.; Medwell, P. R.; Tian, Z. F. Modeling Lifted Jet Flames in a Heated Coflow using an Optimized Eddy Dissipation Concept Model. *Combust. Sci. Technol.* **2015**, *187*, 1093−1109.
(59) Al-Halbouni, A.; Giese, A.; Flamme, M.; Brune, M. Flameless Oxidation and Continued Staged Air Combustion Systems for Gas Turbines. *Int. J. Energy Clean Environ.* **2004**, *5*, 391−405.
(60) Malfa, E.; Venturino, M.; Tota, V. Mathematical Modelling of Flameless Combustion for Micro-CHP System Development. *Proceedings of the 25th Event of the Italian Section of the Combustion Institute*; Rome, June 3−5, 2002.
(61) Sorrentino, G.; Göktolga, U.; De Joannon, M.; Van Oijen, J.; Cavaliere, A.; De Goey, P. An experimental and numerical study of MILD combustion in a cyclonic burner. *Energy Procedia* **2017**, *120*, 649−656.
(62) Dally, B. B.; Masri, A. R.; Barlow, R. S.; Fiechtner, G. J. Instantaneous and mean compositional structure of bluff-body stabilized nonpremixed flames. *Combust. Flame* **1998**, *114*, 119−148.
(63) Sidey, J.; Mastorakos, E. Visualization of MILD combustion from jets in cross-flow. *Proc. Combust. Inst.* **2015**, *35*, 3537−3545.

DOI: 10.1021/acs.energyfuels.8b01064
Energy Fuels 2018, 32, 10228−10241